3. Experimental observability

3.1 Method

The primary experimental aim is to take previously developed model-independent methods for measuring SUSY particle masses (which were developed at standard SUGRA points) and by testing them in the context of a new optimised model, identify where these methods need to be generalised to perform well in both models. Secondarily it is to be shown that, after modifying these methods' treatments of the slepton sector, their performance is sufficient to distinguish between the optimised and standard SUGRA scenarios.

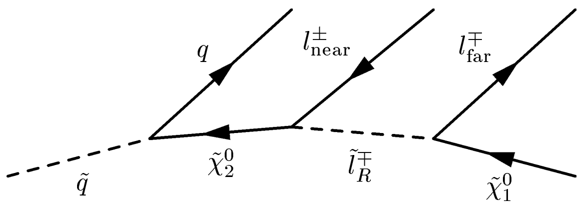

Figure 3: "Sequential" decay.

To accomplish these aims, some model-dependent assumptions have to be made. In this analysis, R-parity is taken to be conserved and certain sparticle decay chains are assumed to exist. In R-parity conserving (RPC) models, SUSY particles are only produced in pairs, and the lightest SUSY particle (LSP) is stable. SUSY events contain two of these LSPs which, being only weakly interacting, escape detection and lead to SUSY events with large amounts of missing transverse energy – the standard signature for RPC models. The fact that these massive particles go missing from all RPC SUSY events means that in these models it is not usually possible to measure particle masses by reconstructing entire decay chains. Thus, as in [1], endpoints in kinematic variables constructed from SUSY decay chains must instead be examined. Specifically, the "sequential" decay mode $\tilde{q}_L \to \tilde{\chi}^0_2 q \to \tilde{l}^{\mp}_R l^{\pm}_{\rm near} q \to \tilde{\chi}^0_1 l^{\mp}_{\rm far} l^{\pm}_{\rm near} q$ (see Figure 3) and the "branched" decay modes $\tilde{q}_L \to \tilde{\chi}^0_2 q \to \tilde{\chi}^0_1 X q \to \tilde{\chi}^0_1 l^{\pm} l^{\mp} q$ (see Figure 4) form the starting point for this investigation.

Figure 4: "Branched" decays through the Z and Higgs bosons.

The kinematic edges used in [1] to identify particle masses at S5 contain:

- l^+l^- edge: This picks out, from the "sequential" decays, the position of the very sharp edge in the dilepton invariant mass spectrum caused by $\tilde{\chi}^0_2 \to l\tilde{l}$ followed by $\tilde{l} \to l\tilde{\chi}^0_1$.

- l^+l^-q edge: In "sequential" decays, the llq invariant mass spectrum contains a linearly vanishing upper edge due to successive two-body decays. Our theoretical model of the l^+l^-q edge is more model independent than that used in earlier studies as it does do not assume any relation between the sparticle masses, other than the hierarchy $0 < m_{\tilde{\chi}_1^0} < m_{\tilde{l}_R} < m_{\tilde{\chi}_2^0} < m_{\tilde{q}}$ necessary for the "seqential" decay chain to exist at all.

- l^+l^-q threshold: This is the non-zero minimum in the "sequential" llq invariant mass spectrum, for the subset of events in which the angle between the two leptons (in the centre of mass frame of the slepton) is greater than $\pi/2$. This translates into the direct cut on m_{ll} described in Section 3.4.1.

- hq edge: This is one of the two instances of the Xq edge. In general, the Xq edge is the upper edge of the distribution of the invariant mass of three visible particles in the "branched" decays of Figure 4. The position of this edge is again determined by two-body kinematics. Depending on the Higgs mass and the mass difference between the $\tilde{\chi}_2^0$ and the $\tilde{\chi}_1^0$, one of the two "branched" decay chains will be strongly suppressed with respect to the other, so typically only one edge will be visible. At S5 the Higgs mode dominates, while the Z mode will dominate at O1.

As detailed later in this analysis, new edges are added to the list above. Two of them are more general versions of other edges treated in [1], while another is entirely new. They are the $l^{\pm}q$ high-, $l^{\pm}q$ low- and M_{T2} edges respectively. To summarise, the overall method we apply in this paper consists of:

- finding a model-independent set of cuts which can be used to select events from which the endpoints of all the kinematic edges may be measured,

- obtaining an estimate of the accuracy with which the edge positions might be determined by an LHC experiment,

- performing chi-squared fits of the expected positions of these edges (as functions of the sparticle masses) to a set of "simulated edge measurements" one might expect from an ensemble of such experiments, and

- interpreting the results as the statistics contribution to model independent sparticle mass measurements of a typical LHC experiment.

Were all squarks to have the same mass, then (with perfect detector resolution and with infinite statistics) the endpoints of the edges listed above would be found at the positions given in Table 4. Note that these positions depend on four unknown parameters, namely the masses of the squark, the slepton and the two neutralinos participating in each decay. The mass of the lightest Higgs boson also appears, but we assume this will already be known or will be obtained by other methods (e.g. [25]) to within 2%.

In a more realistic "non-degenerate squark masses" scenario, every distribution with a squark related edge will actually be a superposition of many underlying distributions (one for each squark mass), each having its edge at a slightly different location. This results in some smearing of the edges, even before detector effects (resolutions, acceptances, jet energy calibrations etc.) are taken into account.

Related edge	Kinematic endpoint
l^+l^- edge	$(m_{ll}^{\max})^2 = (\tilde{\xi} - \tilde{l})(\tilde{l} - \tilde{\chi})/\tilde{l}$
l^+l^-q edge	$(m_{llq}^{\max})^2 = \begin{cases} \max\left[\frac{(\tilde{q}-\tilde{\xi})(\tilde{\xi}-\tilde{\chi})}{\tilde{\xi}}, \frac{(\tilde{q}-\tilde{l})(\tilde{l}-\tilde{\chi})}{\tilde{l}}, \frac{(\tilde{q}\tilde{l}-\tilde{\xi}\tilde{\chi})(\tilde{\xi}-\tilde{l})}{\tilde{\xi}\tilde{l}}\right] \\ \text{except for the special case in which } \tilde{l}^2 < \tilde{q}\tilde{\chi} < \tilde{\xi}^2 \text{ and} \\ \tilde{\xi}^2\tilde{\chi} < \tilde{q}\tilde{l}^2 \text{ where one must use } (m_{\tilde{q}} - m_{\tilde{\chi}_1^0})^2. \end{cases}$
Xq edge	$(m_{Xq}^{\max})^2 = X + (\tilde{q} - \tilde{\xi})\left[\tilde{\xi} + X - \tilde{\chi} + \sqrt{(\tilde{\xi} - X - \tilde{\chi})^2 - 4X\tilde{\chi}}\right]/(2\tilde{\xi})$
l^+l^-q threshold	$(m_{llq}^{\min})^2 = \begin{cases} [\ 2\tilde{l}(\tilde{q}-\tilde{\xi})(\tilde{\xi}-\tilde{\chi}) + (\tilde{q}+\tilde{\xi})(\tilde{\xi}-\tilde{l})(\tilde{l}-\tilde{\chi}) \\ \quad -(\tilde{q}-\tilde{\xi})\sqrt{(\tilde{\xi}+\tilde{l})^2(\tilde{l}+\tilde{\chi})^2 - 16\tilde{\xi}\tilde{l}^2\tilde{\chi}}\ \ ]/(4\tilde{l}\tilde{\xi}) \end{cases}$
$l^{\pm}_{\text{near}}q$ edge	$(m_{l_{\text{near}}q}^{\max})^2 = (\tilde{q} - \tilde{\xi})(\tilde{\xi} - \tilde{l})/\tilde{\xi}$
$l^{\pm}_{\text{far}}q$ edge	$(m_{l_{\text{far}}q}^{\max})^2 = (\tilde{q} - \tilde{\xi})(\tilde{l} - \tilde{\chi})/\tilde{l}$
$l^{\pm}q$ high-edge	$(m_{lq(\text{high})}^{\max})^2 = \max\left[(m_{l_{\text{near}}q}^{\max})^2, (m_{l_{\text{far}}q}^{\max})^2\right]$
$l^{\pm}q$ low-edge	$(m_{lq(\text{low})}^{\max})^2 = \min\left[(m_{l_{\text{near}}q}^{\max})^2, (\tilde{q} - \tilde{\xi})(\tilde{l} - \tilde{\chi})/(2\tilde{l} - \tilde{\chi})\right]$
M_{T2} edge	$\Delta M = m_{\tilde{l}} - m_{\tilde{\chi}_1^0}$

Table 4: The absolute kinematic endpoints of invariant mass quantities formed from decay chains of the types mentioned in the text for known particle masses. The following shorthand notation has been used: $\tilde{\chi} = m^2_{\tilde{\chi}_1^0}, \tilde{l} = m^2_{\tilde{l}_R}, \tilde{\xi} = m^2_{\tilde{\chi}_2^0}, \tilde{q} = m^2_{\tilde{q}}$ and X is m_h^2 or m_Z^2 depending on which particle participates in the "branched" decay.

It is not possible to measure each of the squark masses separately. Consequently the quantity $m_{\tilde{q}}$ in Table 4 will, after being obtained from the "smeared" edges, represent a squark mass *scale* rather than a specific squark mass. In all squark related edges, except the l^+l^-q threshold, the contribution to the outermost part of each edge is provided by the heaviest squarks. In the case of the l^+l^-q threshold, the "true" endpoint is set by the lightest squark. However, if (as at O1 and S5) the other eleven squarks are much heavier (see Table 3), it is easier to measure the contribution coming from them. A strong correlation between $m_{\tilde{q}}$ and the mass of the heaviest squark would therefore be expected.

More work would be required to fully understand the "theoretical" systematic errors including the use of a full simulation of the expected edge positions. Better edge models than those used later in this analysis will definitely be needed to permit measurements of edge positions to be better correlated with functions of the particle masses. Other sources of systematic errors which require further analysis are the detector effects mentioned above, combinatorial backgrounds near the edges and possible cut biases. Such systematic errors can only meaningfully be studied when real data are available.

Although they are beyond the scope of this paper, it is assumed that the above investigations could be performed so as to leave the eventual edge resolutions determined only by statistics and detector resolution. In this analysis, then, all edges are fitted with simple shapes (see Section 3.5) with the intention of extracting only an estimate of the *uncertainty* on the edge position, and not to obtain the edge position itself.

The first four edges listed in Table 4 thus constitute a minimal constraint on the four unknown sparticle mass parameters, which may then be further constrained by the other measurements which follow.

3.2 Other measurements

3.2.1 Near, far, high and low $l^{\pm}q$ edges

In "sequential" decays there are three observable outgoing particles. There are only four different ways of grouping these particles together, and so only four different invariant masses may be formed from them: m_{ll}, m_{llq}, $m_{l_{\rm near}q}$ and $m_{l_{\rm far}q}$. The first two of these, m_{ll} and m_{llq}, may be formed from the observed momenta without knowledge of which lepton was $l_{\rm near}$ and which was $l_{\rm far}$; only the total lepton four-momentum is required. Edges in these invariant mass distributions have already been described. If it were possible to tag the near- and far- leptons separately, the third and fourth invariant mass combinations could also be formed unambiguously, allowing the positions of two more edges, $m^{\rm max}_{l_{\rm near}q}$ and $m^{\rm max}_{l_{\rm far}q}$, to play a part in the final fit. However, such tagging is impossible. If further information is to be gathered from these decays *in a model independent way*, it is then necessary to look for edges in variables (functions of $m_{l_{\rm near}q}$ and $m_{l_{\rm far}q}$) which *are* observable. On an event-by-event basis, then, we define

$$m_{lq({\rm high})} = \max\left(m_{l^+q}, m_{l^-q}\right) \equiv \max\left(m_{l_{\rm near}q}, m_{l_{\rm far}q}\right) \tag{3.1}$$

and

$$m_{lq({\rm low})} = \min\left(m_{l^+q}, m_{l^-q}\right) \equiv \min\left(m_{l_{\rm near}q}, m_{l_{\rm far}q}\right). \tag{3.2}$$

The simplest theoretical predictions for the positions of the corresponding edges, $m^{\rm max}_{lq({\rm high})}$ and $m^{\rm max}_{lq({\rm low})}$, are listed in Table 4, along with the positions of the near- and far-edges. Note that although the position of the high-edge is just the higher of $m^{\rm max}_{l_{\rm near}q}$ and $m^{\rm max}_{l_{\rm far}q}$, the position of the low-edge has a more interesting form. This asymmetry arises because it is not always kinematically possible for the invariant mass of the lepton/quark pair coming from the lower near/far distribution to approach $\min\left[m^{\rm max}_{l_{\rm near}q}, m^{\rm max}_{l_{\rm far}q}\right]$ arbitrarily closely, while simultaneously requiring that this invariant mass is less than that of the other lepton/quark pair.

3.6 Reconstructing sparticle masses

Sparticle masses are reconstructed by performing a chi-squared fit with between four and six free parameters p. The main parameters of the fit are $m_{\tilde{\chi}_1^0}$, $m_{\tilde{l}}$, $m_{\tilde{\chi}_2^0}$ and $m_{\tilde{q}}$. Where appropriate, m_h and m_Z also appear as fit parameters, although if they do, they are strongly constrained (particularly in the case of the Z) by present LEP measurements or expected LHC errors (0.0077% and 2.0% respectively).

The chi-squared, as a function of the free parameters p, is then formulated as:

$$\chi^2(p) = \sum_1^n \frac{(O_i^{\mathrm{sm}} - O_i(p))^2}{{\sigma_i}^2}, \tag{3.8}$$

where $O_i^{\mathrm{sm}} = O_i(p_{\mathrm{model}}) + \sigma_i X_i$ are n "smeared observables", $X_i \sim N(0,1)$ are the n random variables from the Normal distribution (with mean 0 and standard deviation 1) which accomplish the smearing, σ_i is the anticipated statistical error for the i^{th} observable (approximated by the fit error listed in Table 5), and $O_i(p)$ is the value one would expect for the i^{th} observable given the parameters p (for examples see Table 4). p_{model} indicates the actual masses of the sparticles in the particular model being considered. The results of the fit, p_{fit}, are then those which minimise the chi-squared. p_{fit} may be interpreted as the sparticle masses which might be reconstructed by an LHC experiment after obtaining $100\mathrm{fb}^{-1}$ at high luminosity, with the X_i parametrising the experimental errors. In order to determine the accuracy with which this reconstruction can be performed, the above fitting process is repeated many times for different values of the X_i, producing the distributions of reconstructed particle masses which follow.

	Fractional RMS $\sqrt{\overline{\varepsilon_p^2}}$		Fractional mean $\overline{\varepsilon_p}/10^{-3}$		Reconstruction width $\sqrt{\overline{(m_p - \overline{m_p})^2}}$	
p	S5	O1	S5	O1	S5	O1
$\tilde{\chi}_1^0$	0.140	0.175	11.4	8.0	17 GeV	22 GeV
$\tilde{l}_R$	0.112	0.091	8.8	5.7	17 GeV	20 GeV
$\tilde{\chi}_2^0$	0.074	0.084	6.0	5.3	17 GeV	20 GeV
$\tilde{q}$	0.034	0.047	2.7	2.4	22 GeV	29 GeV

Table 6: RMS and mean values, for each of the particles p, of the fractional mass-error distributions (ε_p) in Figures 13 and 14. Also shown are the widths of the distributions of the reconstructed particle masses (from Figures 11 and 12).

Figures 11 and 12 show the probability distributions expected for the reconstructed $\tilde{\chi}_1^0$, $\tilde{l}$, $\tilde{\chi}_2^0$ and $\tilde{q}$ masses, while Figures 13 and 14 show the corresponding fractional errors, ε_p, for the same quantities. All are approximately Gaussian and have reassuringly small tails. Statistics summarising these plots (widths, means and RMS values) are listed in Table 6.

It may be seen that in both O1 and S5 the widths of the mass distributions for all four particles are very similar. This is because, in localized regions of parameter space, the edges tend to constrain mass differences far better than absolute masses. Evidence of this may be seen in Figure 15 which shows the scatter of reconstructions in the $m_{\tilde{\chi}_1^0}$-$m_{\tilde{l}_R}$

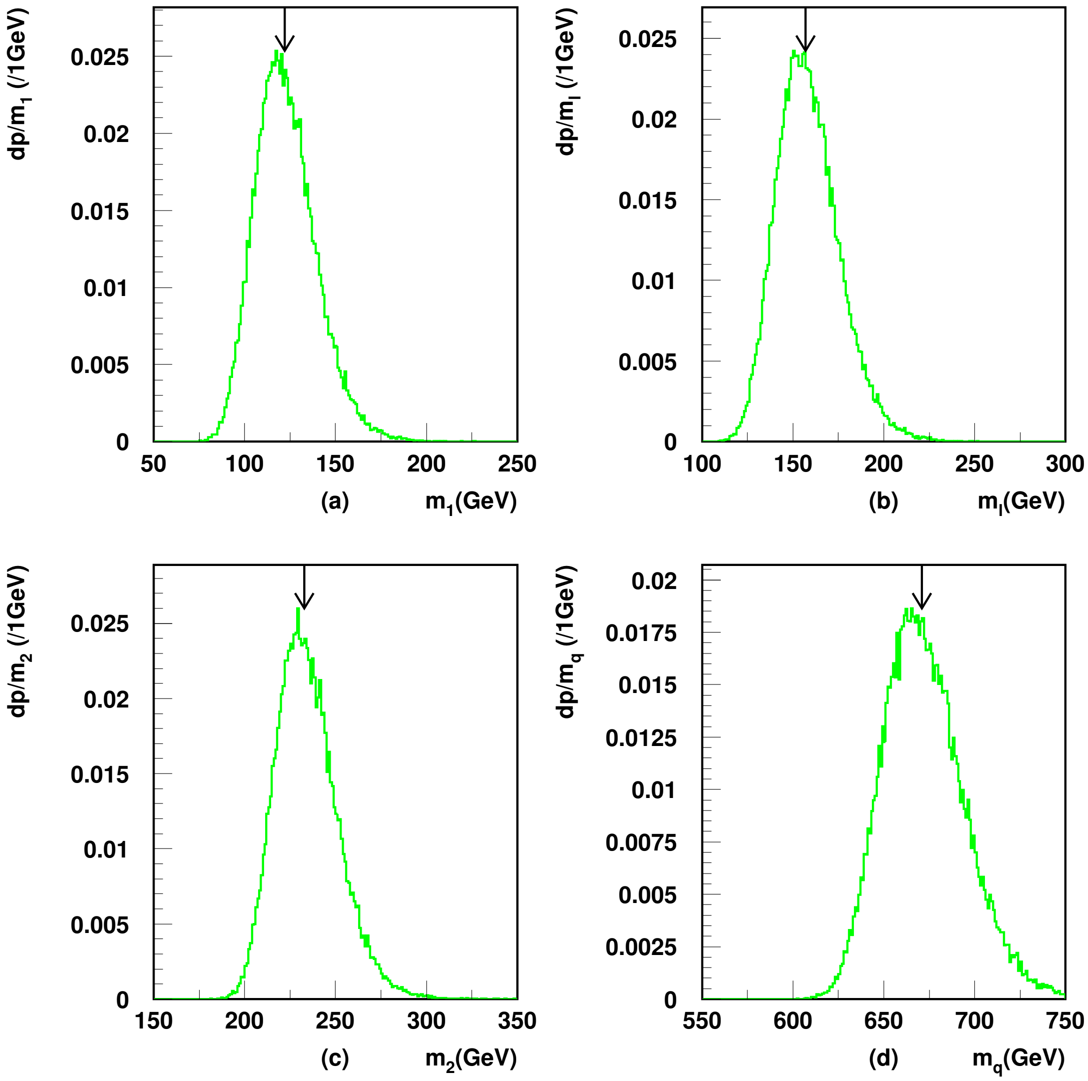

Figure 11: Reconstructed $\tilde{\chi}_1^0$, $\tilde{l}$, $\tilde{\chi}_2^0$ and $\tilde{q}$ masses at S5. The small arrows indicate the masses used as the input parameters, $p_{\rm model}$.

plane. It is interesting to note that *without* the M_{T2} constraint at O1, the fit's chi-squared commonly has two distinct and competing comparable minima – one at high and one at low values of $m_{\tilde{l}_R}$. The simultaneous existence of these minima is a direct consequence of putting the near and far $l^{\pm}q$ edges on an equal footing in this analysis, allowing more than one interpretation for each of the high and low edges. The need to resolve this kind of ambiguity in model-independent investigations of this type illustrates the importance of establishing reliable model-independent ways of measuring the absolute scale of $m_{\tilde{l}_R} - m_{\tilde{\chi}_1^0}$ (or a related quantity) even if only to an accuracy of 20-30%.

The clear gap between the reconstruction regions for O1 and S5 in Figure 15 supports the original claim that, systematic errors permitting, it will be possible to distinguish between the two scenarios.

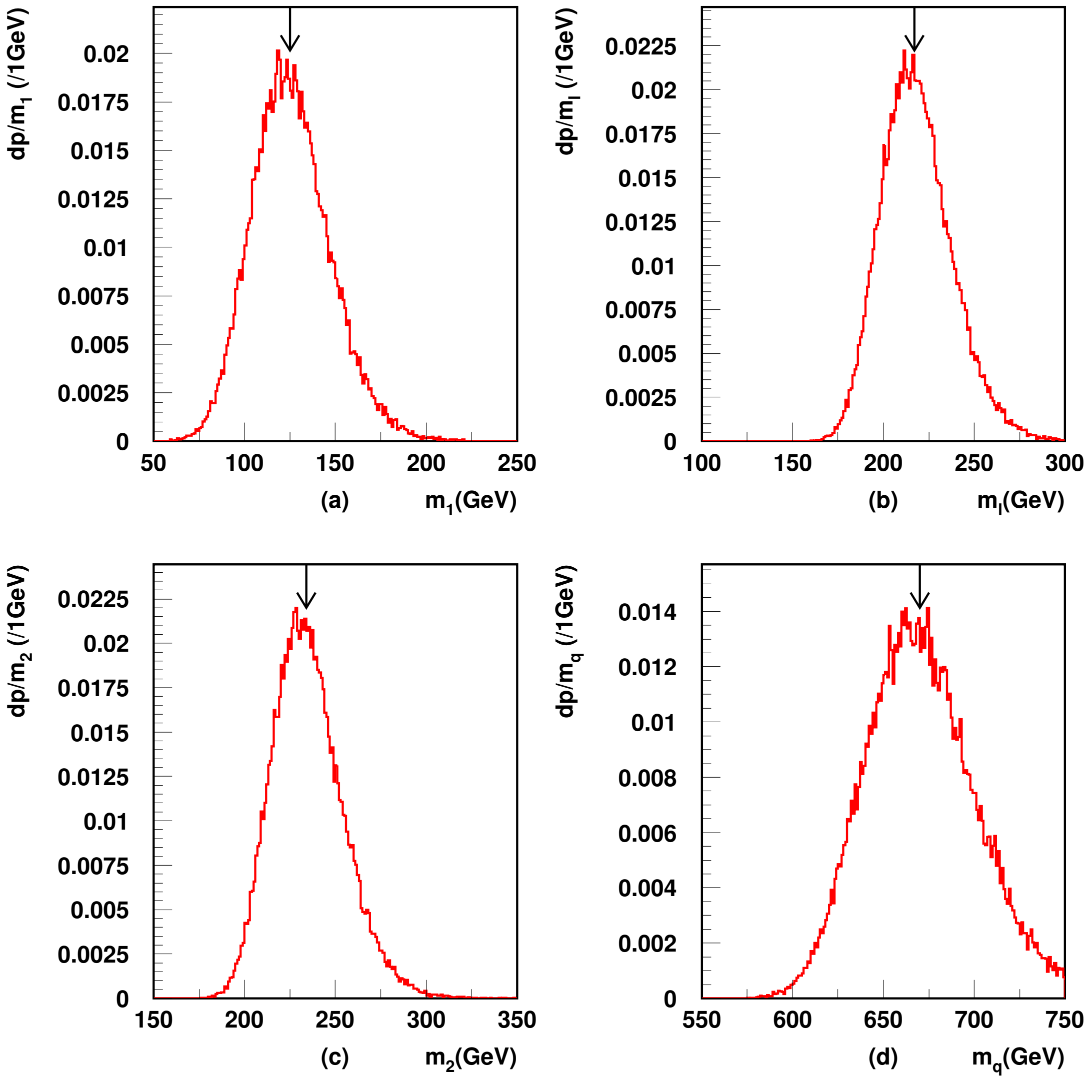

Figure 12: Reconstructed $\tilde{\chi}_1^0$, $\tilde{l}$, $\tilde{\chi}_2^0$ and $\tilde{q}$ masses at O1. The small arrows indicate the masses used as the input parameters, $p_{\rm model}$.

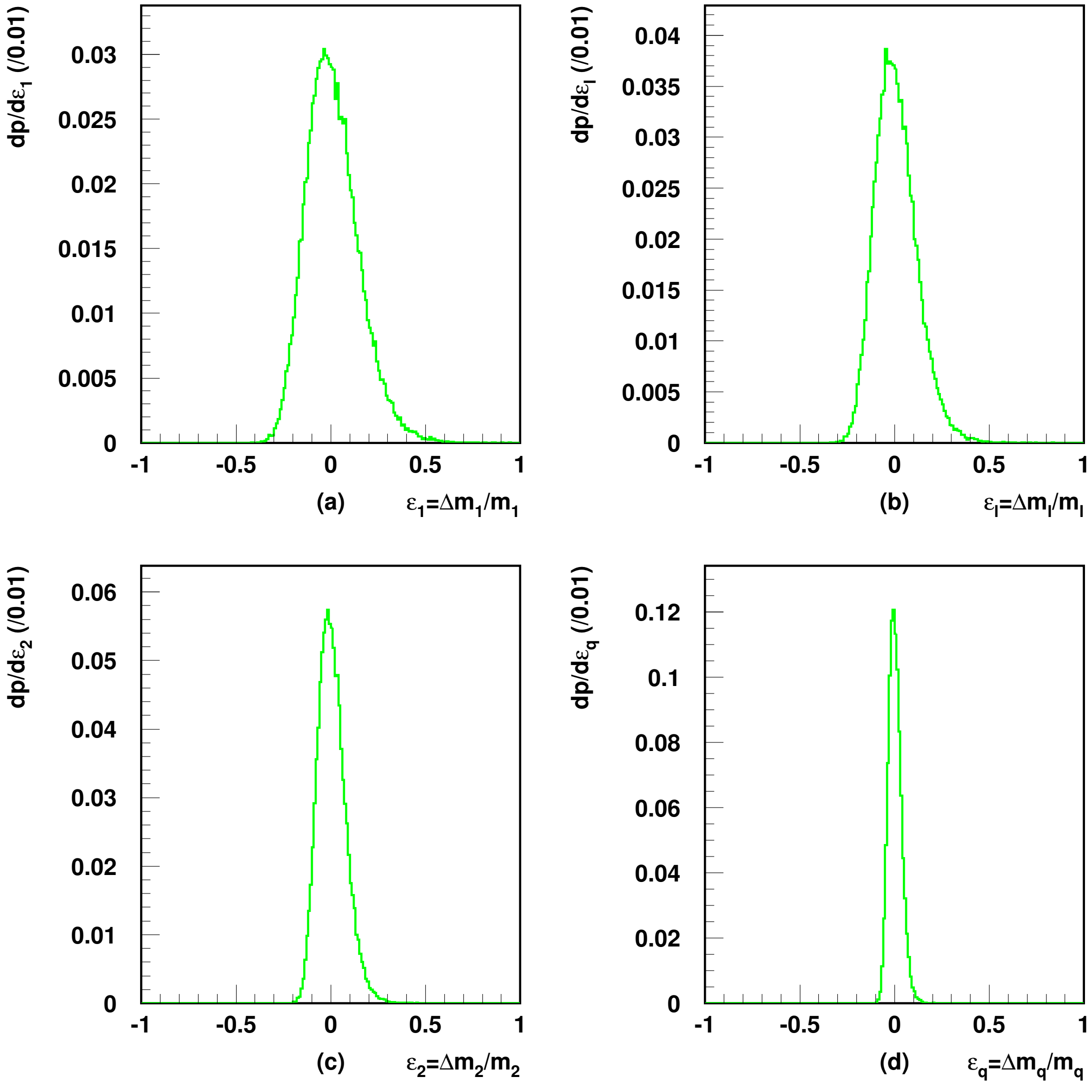

Figure 13: Fractional errors in reconstructed $\tilde{\chi}_1^0$, $\tilde{l}$, $\tilde{\chi}_2^0$ and $\tilde{q}$ masses at S5.

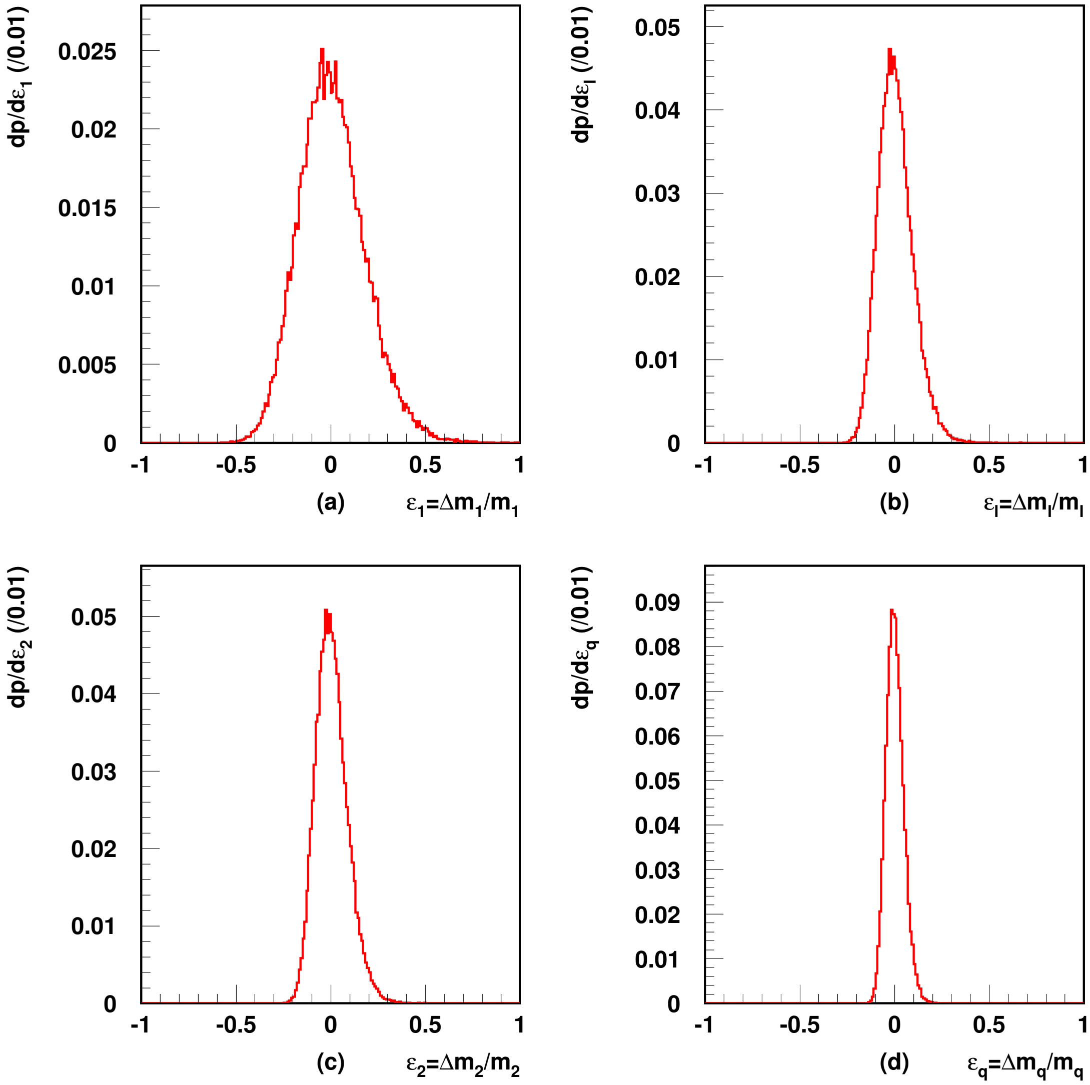

Figure 14: Fractional errors in reconstructed $\tilde{\chi}_1^0$, $\tilde{l}$, $\tilde{\chi}_2^0$ and $\tilde{q}$ masses at O1.

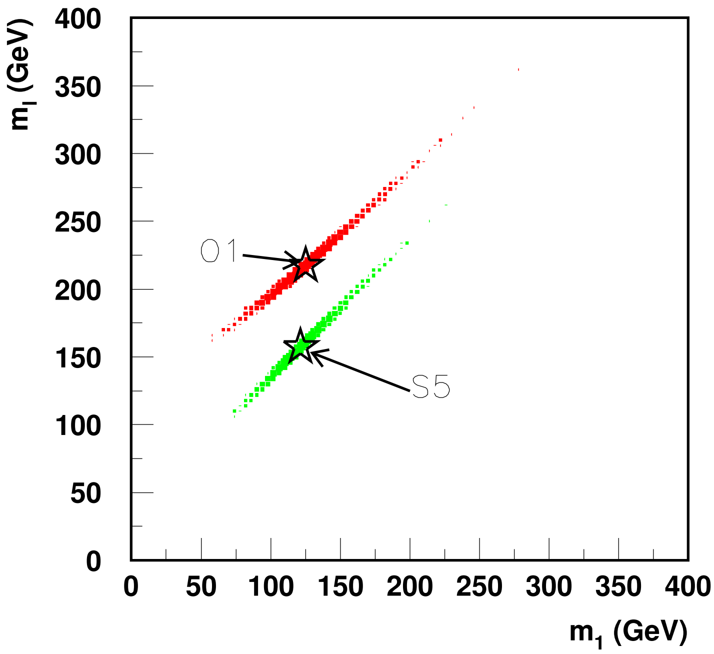

Figure 15: Reconstructed $m_{\tilde{l}}$ versus $m_{\tilde{\chi}_1^0}$ for $O1$ and $S5$. The stars show the true masses for each model.